Low Temperature Physics/Fizika Nizkikh Temperatur, 2017, v. 43, No. 8, pp. 1229–1235

Effect of doping and annealing on crystal structure and magnetic properties of $La_{1-x}Ag_xMnO_3$ magnetic nanoparticles

M. Zentková[1], M. Antoňák[1], M. Mihalik[1], M. Mihalik, Jr.[1], M. Vavra[1,2], V. Girman[2], M. Fitta[3], and J. Briančin[4]

[1]*Institute of Experimental Physics SAS, Watsonova 47, 04001 Košice, Slovakia*

[2]*Faculty of Sciences P.J. Šafarik University, Mozyesova 11, Košice, Slovakia*

[3]*The Henryk Niewodniczanski Institute of Nuclear Physics PAN, ul. Radzikowskiego 152, 31-342 Kraków, Poland*

[4]*Institute of Geotechnics SAS, Watsonova 45, Košice, Slovakia*
E-mail: zentkova@saske.sk

Received February 8, 2017, published online June 26, 2017

We study crystal structure and magnetic properties of $La_{1-x}Ag_xMnO_3$ nanopowders prepared by glycine — nitrate method. The particle size and crystal structure were modified by heat treatment. The average size of particle varies from about 26.6(4) nm for as prepared sample to 63.3(9) nm for annealed sample at 900 °C/2h. Crystal structure changes from orthorhombic *Pnma* to rhombohedral $R\bar{3}c$ after annealing at 600 °C/2h. The saturated magnetization μ_s and the Curie temperature T_C increase with annealing; T_C is more than doubled after annealing at 600 °C/2h. Exchange bias phenomena were first observed on nanoparticles with orthorhombic crystal structure. The hysteresis loop shifts in horizontal and vertical direction after cooling in magnetic field $\mu_0 H_{cf} \neq 0$ through T_C. The values of exchange bias field $\mu_0 H_E$, coercive field $\mu_0 H_c$, remnant asymmetry μ_E and coercive magnetization μ_c increase with increasing value of cooling field $\mu_0 H_{cf}$. In addition the training effect was observed.

PACS: **75.50.–y** Studies of specific magnetic materials;
75.50.Tt Fine-particle systems; nanocrystalline materials;
75.47.Lx Magnetic oxides;
75.30.Kz Magnetic phase boundaries.

Keywords: crystal structure, magnetic nanoparticles, doping, annealing.

Introduction

The mixed-valence manganese oxides of the general formula $La_{1-x}A_xMnO_3$ (A is a divalent ion like Ca, Sr, Ba and Pb) are a subject of interest due to a desire to understand and exploit the large negative magneto-resistance and magnetocaloric effects [1,2]. The ratio of Mn^{3+}/Mn^{4+} is an important factor to show insulator-to-metal (I–M) transition and ferromagnetic phase transition in manganites. Group of $La_{1-x}Ag_xMnO_3$ manganites provides a series of new oxides to study magnetocaloric effect [3–5] insulator-to-metal transition and colossal magnetoresistance [6] at room temperature.

Recently the exchange bias (EB) effect in mixed-valent manganites having distorted perovskite structure was reported in a spontaneously phase separated system $Pr_{1/3}Ca_{2/3}MnO_3$ [7] which stimulated new interest for study of the EB effect in structurally single-phase compounds. EB effect was discovered more than 55 years ago, by Meiklejohn and Bean on Co/CoO core–shell nanoparticles [8], and its characteristic signature is the horizontal shift of the centre of magnetic hysteresis loop from its normal position at $\mu_0 H = 0$ to $\mu_0 H_E \neq 0$ and vertical shift which can be characterised by remnant asymmetry μ_E. EB usually occurs in systems which are composed by an antiferromagnet (AFM) that is in atomic contact with a ferromagnet (FM) after the system is cooled, below the Néel and respective Curie temperatures T_N and T_C, in an external cooling field $\mu_0 H_{cf}$. EB phenomena were observed in various materials like Laves phases, intermetallic compounds and alloys, binary alloys, Heusler alloys [9] or on layered bulk fluorometallo complex [10] where different

aspects of magnetism were focused from the EB effect. In the case of a fine particle system the surface to volume ratio becomes significantly large compared to the bulk counterpart. In such a case the surface effect dominates over the core. In our paper we study crystal structure, magnetic properties and the effect in $La_{1-x}Ag_xMnO_3$ system of nanoparticles. The preliminary results of our study were presented in [11].

Experimental details

Preparation of nanopowders followed the glycine-nitrate method, where glycine was used as fuel and nitrates as oxidants [12]. The size of nanoparticles, crystal structure and magnetic properties were modified by the annealing in muffle furnace 300 °C/2h, 600 °C/2h and 900 °C/2h. The morphology of nanoparticles and their size distribution was studied on powders by scanning electron microscope (SEM) MIRA3 TESCAN. The average size of particles was determined with the help of program ImageJ. An additional characterisation of prepared sample was performed by transmission electron microscopy (TEM) using a scanning transmission electron microscope JEOL JEM 2100F UHR. Microscope operates with accelerating voltage 80 kV to 200 kV and also enables structure observations at atomic level (HRTEM). Colloids, mixture of the sample and acetone, were prepared for TEM investigation and subsequently a droplet of the colloid was placed on a grid covered by carbon. These particles were covered by carbon layer in next step. The x-ray powder diffraction (XRPD) measurements have been carried out on the X'Pert PRO diffractometer with Cu-K_α radiation (λ_1 = 1.54056 Å, λ_2 = 1.54440 Å) and the XRPD patterns were identified with the FullProf program based on the Rietveld method [13]. The particle size was estimated from XRPD records using microstructural analysis within FullProf package, where each reflection is analyzed with the aim to determine the average particle size. All magnetization measurements were performed by MPMS XL−5 (Quantum Design) apparatus in the temperature range from 1.8 K to 380 K and in magnetic field up to 5 T.

Results and discussion

Crystal structure. XRPD structure analysis revealed that as prepared samples and the samples annealed at 300 °C crystalize in orthorhombic crystal structure (space group Pnma). The crystal structure building blocks MnO_6 are deformed by Jahn Teller distortion and are tilted. The samples annealed at 600 °C and 900 °C crystallize in rhombohedral structure (space group $R\bar{3}c$). Typical XRPD record for samples with *Pnma* and $R\bar{3}c$ symmetry are displayed on Figs. 1, 2. Secondary phase arising due to the presence of synthesis residua can be seen in XRD spectra (Fig. 1) for as prepared sample but vanishes after heat treatment. Less than 5 % of silver is detected by the analysis of XRPD spectra for the whole series of samples (Figs. 1, 2). It is generally accepted

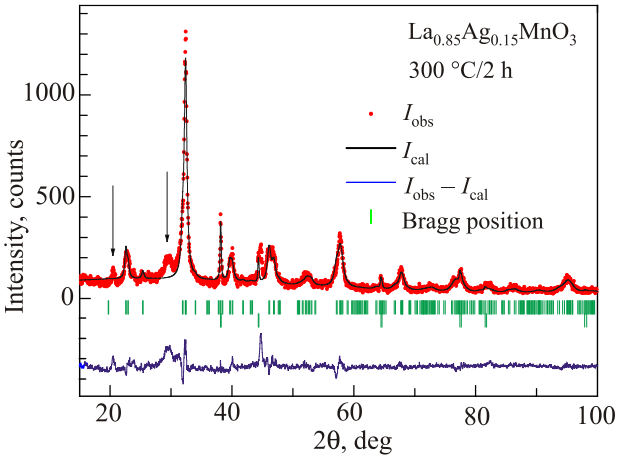

Fig. 1. (Color online) X-ray pattern of $La_{0.85}Ag_{0.15}MnO_3$ annealed at 300 °C with orthorhombic phase, unknown phase (see arrows) and Ag.

that the presence of silver does not influence magnetic properties of investigated samples. The lattice parameters are summarized in Table 1. The XRPD measurements indicate that the average particle size is constant in orthorhombic phase, but increases in rhombohedric phase with annealing temperature (x = 0.10: D = 29 nm, 25 nm, 62 nm, 64 nm; x = = 0.15: D = 29 nm, 25 nm, 62 nm, 64 nm; x = 0.15: D = = 24 nm, 30 nm, 63 nm, 101 nm; x = 0.20: D = 25 nm, 24 nm, 49 nm, 135 nm, where x equals Ag doping, D — average particle size of as prepared sample and annealed samples at 300 °C, 600 °C and 900 °C.

SEM analysis revealed that the prepared samples in the form of fine powder form agglomerates having spherical shape, hollow inside, and possibly the cover is constituted by nanoparticles (Fig. 3(a)). To determine the size of the nanoparticles, we used an image analysis of the SEM photo. From suitable pictures, in which the nanoparticles can be distinguished in agglomerates, we determined the parti-

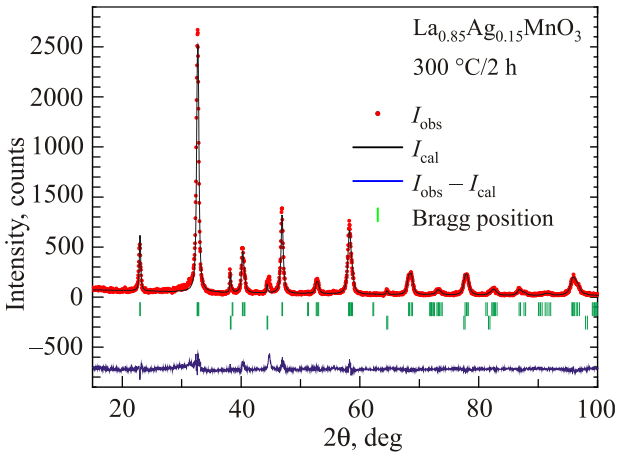

Fig. 2. (Color online) X-ray pattern of $La_{0.85}Ag_{0.15}MnO_3$ annealed at 600 °C indicates rhombohedral phase and Ag.

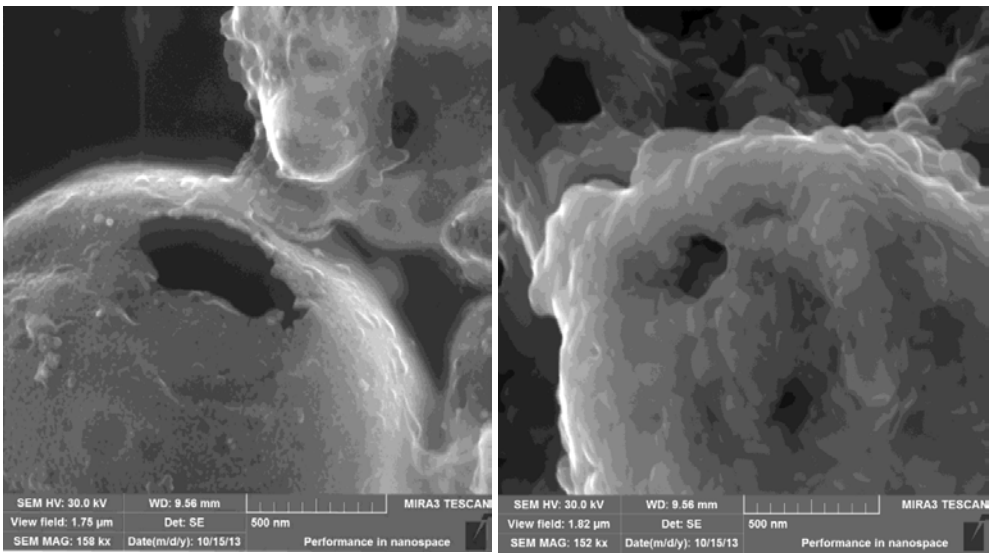

Fig. 3. SEM images of $La_{0.85}Ag_{0.15}MnO_3$ show aggregates as it is demonstrated for as prepared sample (left) and sample annealed at 900 °C (right).

cle size by measurements of diameters of all visible nanoparticles gradually in the vertical and horizontal direction (relative to the SEM picture). From the measured data, we created a histogram of statistical distribution of the nanoparticles in a certain size range as it is demonstrated in Fig. 4. To determine the final average size of the nanoparticles, we used lognormal distribution and we have determined the average particle size as the maximum of this distribution function. The average particle size is 26.6(4) and 63.3(9) nm for sample as prepared and annealed at 900 °C, respectively.

TEM study on the same samples confirmed that all samples consist from agglomerates of nanoparticles as it is shown for sample annealed at 300 °C (Fig. 5). One grain from this sample was studied by HRTEM (Fig. 6), directly showing the MnO_6 octahedrons on the atomic level. The size of particles depends on annealing and corresponds with size of nanoparticles determined by scanning electron microscopy and XRPD. The smallest particles have size between 10 and 15 nm; typically have character of single crystals or sometimes consists of several sub-grains as it was revealed by HRTEM study (Fig. 7). The shape of particles is spherical (Fig. 7) or cylindrical (Fig. 8). Spherical shape can be just different projection of cylindrical sample.

Magnetic properties. Our measurements revealed that all samples undergo a paramagnetic (PM) to ferromagnetic (FM) transition at the Curie temperature T_C. The temperature dependences of magnetization in zero field cooled (ZFC) and field cooled (FC) regimes are shown in Fig. 9. for as prepared $La_{0.80}Ag_{0.20}MnO_3$ sample. The hysteretic behavior between magnetization measurements performed in ZFC and FC regimes for low applied magnetic fields is typical feature of all samples. Bifurcation temperature T_b is comparable with the Curie temperature T_C and even is a

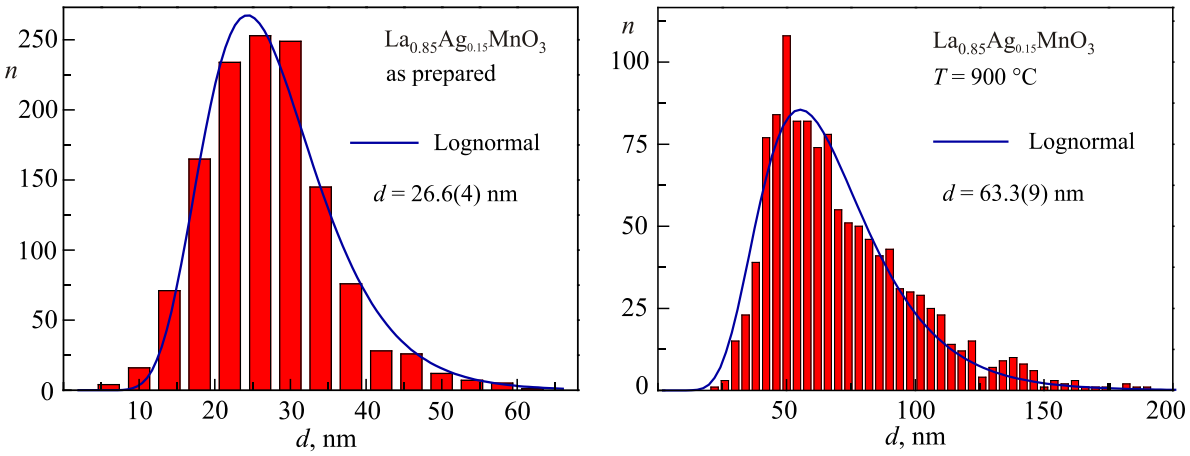

Fig. 4. (Color online) The particle size distribution for different samples of $La_{0.85}Ag_{0.15}MnO_3$. The binning of the data is 4 nm in all cases.

Table 1. Lattice parameters of $La_{1-x}Ag_xMnO_3$

Composition x	Status	a, Å	b, Å	c, Å	% of Ag
0.20	as prepared	5.654(1)	7.751(1)	5.539(1)	4.32
	300 °C	5.645(1)	7.752(1)	5.532(1)	5.43
	600 °C	5.5060(1)	5.5060(1)	13.3612(1)	4.31
	900 °C	5.5077(1)	5.5077(1)	13.3543(1)	2.82
0.15	as prepared	5.643(1)	7.754(1)	5.529(1)	2.62
	300 °C	5.605(1)	7.756(1)	5.530(1)	4.95
	600 °C	5.5027(1)	5.5027(1)	13.3596(1)	2.29
	900 °C	5.5106(1)	5.5106(1)	13.3507(1)	0.75
0.10	as prepared	5.652(1)	7.747(1)	5.539(1)	1.34
	300 °C	5.641(1)	7.751(1)	5.533(1)	3.22
	600 °C	5.504(1)	5.5037(1)	13.3544(1)	0.27
	900 °C	5.513(1)	5.5133(1)	13.3446(1)	0.12

little bit higher for as prepared samples. The Curie temperature was determined as a minimum on $d\mu/dT(T)$ dependence. High temperature magnetic susceptibility χ follows the Curie–Weiss law $\chi = C/(T - \theta)$ for all samples in temperature region high enough above T_C (C is the Curie constant and θ is paramagnetic Curie–Weiss temperature) as it is demonstrated for as prepared sample with $x = 0.20$ (Fig. 10). The curvature of $1/\chi(T)$ in the range between 100 and 150 K can indicate presence of different short range ordering (clusters) in the vicinity of T_C. Substitution of Ag for La and subsequent heat treatment increase T_C reaching the maximal value 307 K for sample with $x = 0.2$ annealed at 900 °C/2h (Fig. 11). In this case the shape of magnetization $\mu(T)$ and inverse susceptibility $1/\chi(T)$ is typical for ferromagnetic materials. The paramagnetic Curie temperature increases with annealing from $\theta = 110$ K to 113 K and finally to 267 K on the sample with $x = 0.15$ and T_C increases from 107 K to 121 K and then to 268 K for as prepared, 300 °C/2h and 600 °C/2h annealed particles of $La_{0.85}Ag_{0.15}MnO_3$, respectively. The same tendency we have found on samples with $x = 0.10$ and 0.20. The magnetization loop has S-shape, is relatively narrow and magnetization does not completely saturate even at 5 T as it is demonstrated in Fig. 12.

The increase of T_C and θ with annealing for the annealing temperatures up to 300 °C we attribute to oxidation generating higher content of Mn^{4+} which increases ferromagnetic interaction via double exchange interaction. Evidence for enhanced oxidation was provided by iodometric titration and TG measurements. Annealing at 600 °C and 900 °C resulted to the change of the crystal structure from orthorhombic one to the rhombohedral one. In the orthorhombic structure the MnO_6 octahedrons are tilted with respect to each other and the Mn–O–Mn angle is within interval 152–155 deg for all concentrations. On the other hand, in the rhombohedral structure the MnO_6 octahedrons are not tilted and the Mn–O–Mn angle is 180 deg, which is given by the crystal symmetry. Since the magnetic interaction in this system is superexchange, its strength depends on the cosine of the Mn–O–Mn angle. For that reason the rhombohedric samples have much higher ordering temperatures than their orthorhombic counter-parts. Changes of magnetic properties which were induced by increasing of silver content x

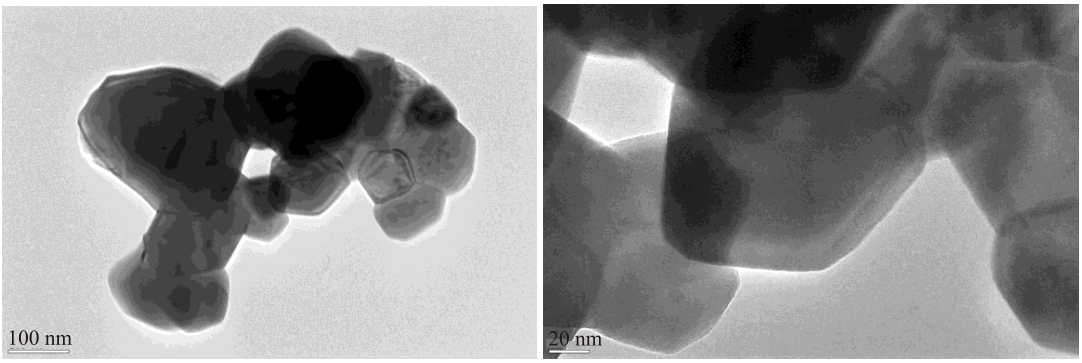

Fig. 5. TEM images of particle aggregates for annealed sample at 300 °C/2h.

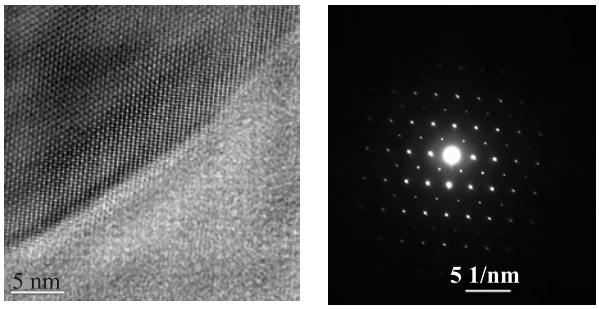

Fig. 6. HTEM image of an individual particle for annealed sample at 300°C/2h and the electron diffraction pattern.

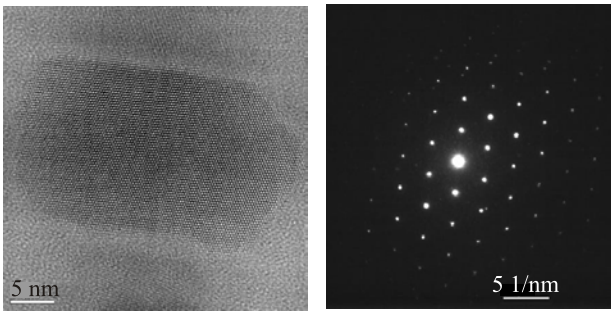

Fig. 8. HTEM image and the electron diffraction pattern of a cylindrical particle for annealed sample at 300 °C/2h are shown for the case of perfect crystal structure (left).

are much smaller than these drastic changes of the crystallographic structure induced by annealing. The effective magnetic moment μ_{eff} changes by non-monotonic way with annealing; at first, μ_{eff} decreases from 4.74 μ_B to 4.14 μ_B and then increases to 4.53 μ_B for as prepared, 300 °C/2h and 600 °C/2h annealed samples with $x = 0.15$. The decrease of μ_{eff} can be understood assuming oxidation resulting in higher content of Mn^{4+} in samples and smaller moment can be obtained by the combination of magnetic moments of Mn^{3+} (4.90 μ_B), Mn^{4+} (3.87 μ_B). Annealing at 600 °C/2h will again increase Mn^{4+} content in samples but the effective moment is smaller now. Relation between gradual oxidation and decreasing moment is now not so straightforward and seems to be misleading but the change of crystal structure from *Pnma* to $R\bar{3}c$ has to be taken into account.

Two magnetization hysteresis loops which were measured on as prepared sample with $x = 0.15$ are displayed in Fig. 13. First of them was obtained after cooling down in zero magnetic field. Initial magnetization curve starts from zero remnant magnetization and the hysteresis loop is symmetric in respect to zero point of coordinates. Before measurement of second loop the sample was exposed to static magnetic field $\mu_0 H_{cf}$ with induction of 1 T and cooled from 120 K through T_C down to 2 K. This procedure gives rise to displacement of the magnetic hysteresis loop, which is the typical manifestation of the exchange bias (EB) effect. The loop is pinned on vertex in the region of negative magnetization, is tilt and shifted in horizontal and vertical direction. The horizontal shift of the loop is usually expressed by exchange bias field $H_E = (H_{c+}–H_{c–})/2$ and vertical shift is described by M_E, which is defined as difference of saturated magnetization [9]; H_{c+} and $H_{c–}$ is coercive field on positive and negative axes. In the case that hysteresis loops are not very rectangular another parameter, the remnant asymmetry $\mu_E = (\mu_{r+} - \mu_{r–})/2$, is frequently used [14]; μ_{r+} and $\mu_{r–}$ is remnant magnetization on positive or negative axis. The heat treatment at 300 °C leads to damping of EB phenomena. Despite of the fact that the coercive magnetization $\mu_c = (\mu_{r+}+\mu_{r–})/2$ increases from 0.130 μ_B to 0.246 μ_B, horizontal shift of hysteresis loop is reduced and vertical shift is nearly unchanged as it was found on sample with $x = 0.15$. EB phenomena were observed on all samples which adopt orthorhombic crystal structure and comparison of EB effect for as prepared samples with different content of x is shown in Fig. 14. Saturated magnetization at 5 T decreases with x and horizontal and vertical shift of hysteresis loops is re-

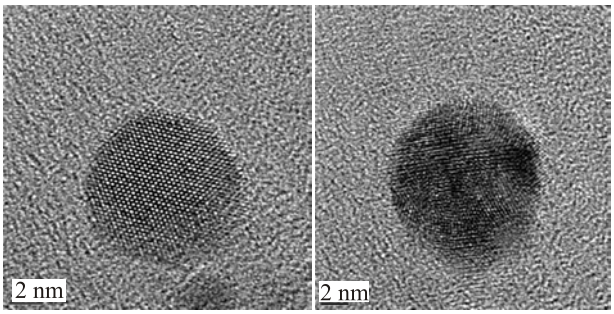

Fig. 7. HTEM images of a spherical particle for annealed sample at 300 °C/2h are shown for the case of perfect crystal structure (left) and for distorted structure (right).

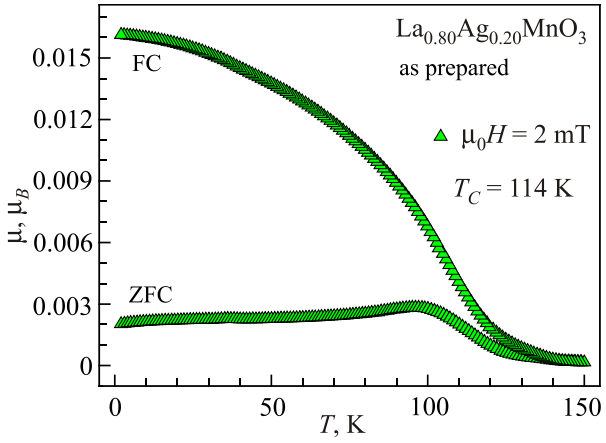

Fig. 9. (Color online) ZFC and FC magnetization curves for as prepared sample.

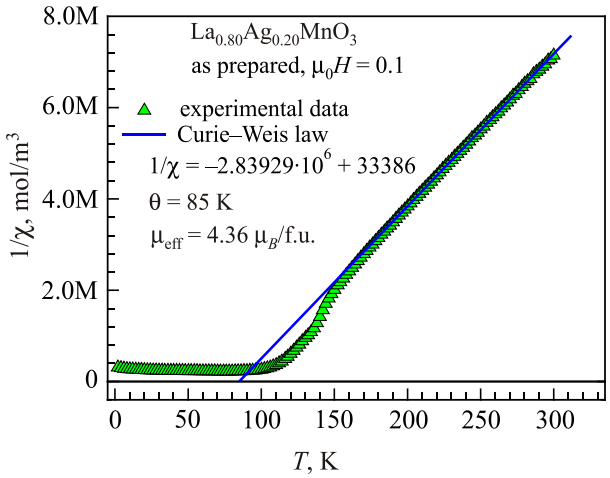

Fig. 10. (Color online) Inverse susceptibility is shown for as prepared sample.

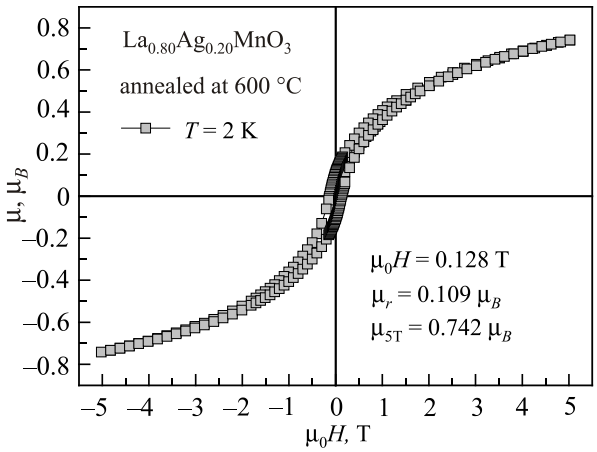

Fig. 12. Hysteresis loop for annealed sample at 600 °C.

markable. All characteristic parameters of EB effect which were obtained in magnetic fields with induction ±9 T are summarised in Fig. 15 which shows effect of cooling field $\mu_0 H_{cf}$ on EB phenomena. All studied parameters have tendency of saturation for relatively low field of about $\mu_0 H_{cf}$ = = 0.1 T. The heat treatment at 300 °C leads to reduction of coercive force H_c and bias field H_E, on the other hand the coercive magnetization μ_c and remnant asymmetry μ_E increase. The difference between subsequent magnetization reversal loops which were measured after cooling in $\mu_0 H_{cf}$ = 1 T, the training effect, is shown in Fig. 16 for $La_{0.85}Ag_{0.15}MnO_3$ sample annealed at 300 °C. Measurement of magnetization reversal loop was repeated 7 times at 2.5 K. It was shown that in generally the parameters H_E, μ_E depend on H_{cf}, H_{max} [15] and for AFM/FM systems in the case of subsequent magnetization reversal loops the FM shell generates spin configuration relaxation on the AFM interface leading to state of equilibria (Landau–Khalatnikov formula [15]):

$$H_E(n+1) = H_E(n) - \gamma\left[H_E(n) - H_{E\infty}\right]^3,$$

$$\mu_E(n+1) = \mu_E(n) - \gamma\left[\mu_E(n) - \mu_{E\infty}\right]^3,$$

where γ is sample dependent constant. In our case both parameters H_E and μ_E describing the horizontal and vertical shift of loop decrease with consecutive number of cycles and reach stable values. In conclusion, EB phenomena were observed on ferromagnetic $La_{1-x}Ag_xMnO_3$ nanopowders (x = 0.10, 0.15 and 0.20) with average size of about 25 nm which adopt orthorhombic crystal structure (space group *Pnma*). All parameters describing EB effect have tendency of saturation in relatively low field of about $\mu_0 H_{cf}$ = 0.1 T. The heat treatment at 300 °C leads to reduction of coercive force H_c and bias field H_E, on the other hand the coercive magnetization μ_c and remnant asymmetry μ_E increase. Both parameters H_E and μ_E describing the horizontal and vertical shift of loop decrease with consecutive number of cycles in training effect. Heat treatment

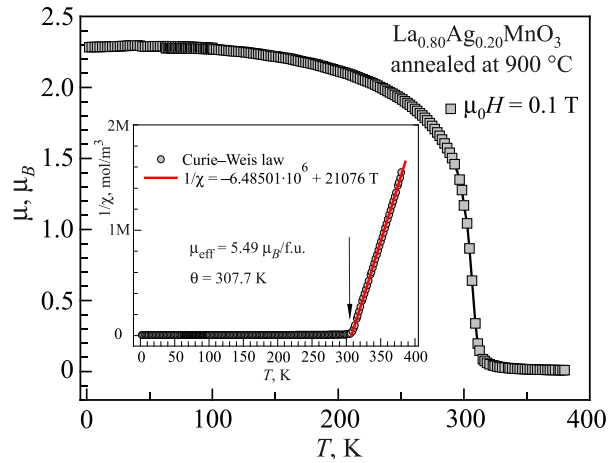

Fig. 11. (Color online) Temperature dependence of magnetization and inverse susceptibility for annealed sample at 600 °C.

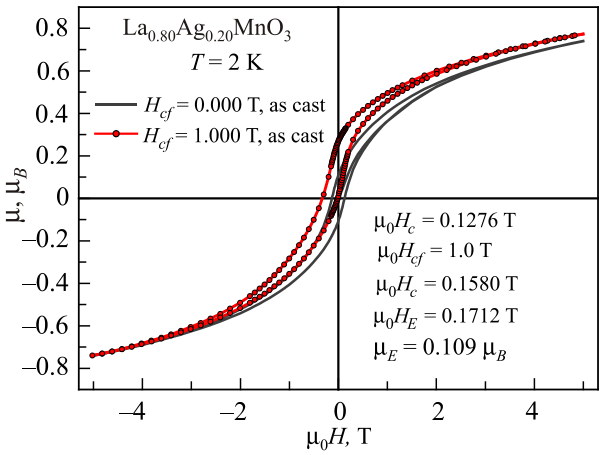

Fig. 13. (Color online) EB effect is shown for as prepared sample with x = 0.15.

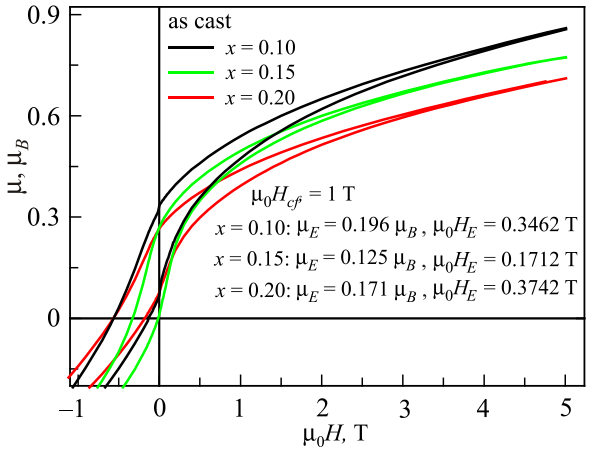

Fig. 14. (Color online) EB effect is compared on as prepared sample with different chemical composition.

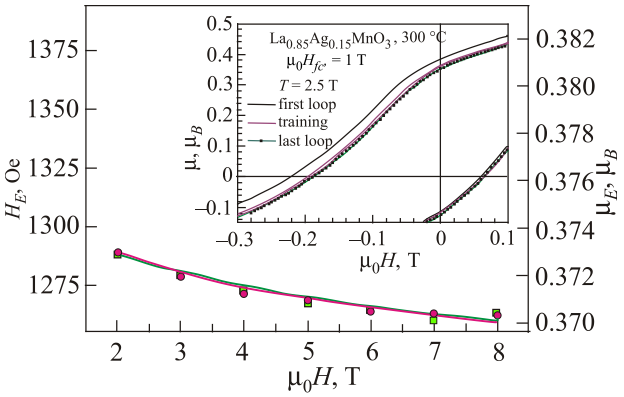

Fig. 16. (Color online) Training effect was studied on sample with $x = 0.15$.

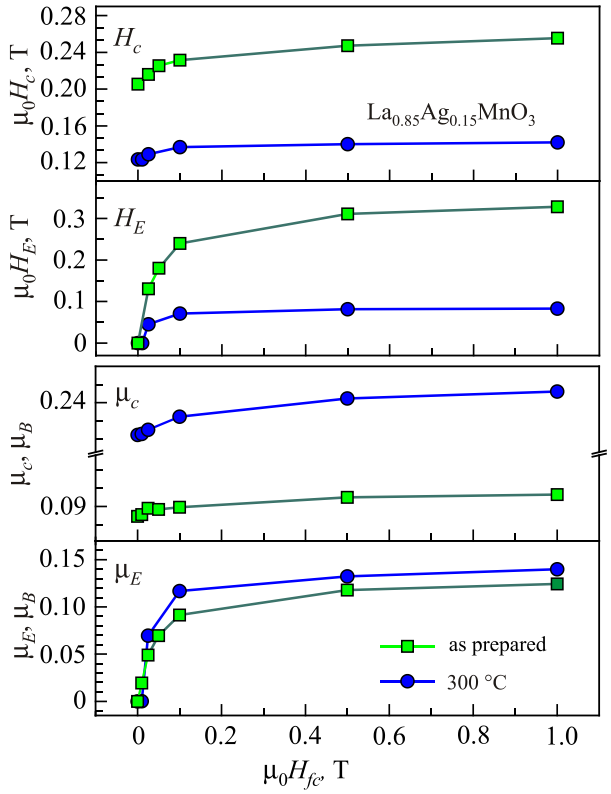

Fig. 15. (Color online) Summary of EB effect which was measured in fields with induction up to 9 T on the sample with $x = 0.15$.

at 600 °C/2 h increases the average size of nanoparticles to 55 nm, crystal structure changes to rhombohedral structure (space group $R\bar{3}c$) and EB effect vanishes. Our results suggest that surface effects and core shell model can explain EB phenomena in this case because it is well known that surface effect is important on particle with average size smaller than 50 nm.

This work was supported by the project ERDF EU, No. ITMS26220120005, VEGA 2/0132/16 and MAD SK-PL 16.

1. J.M.D. Coey, T. Venkatesan, A.J. Millis, J.R. Cooper, P.C. Riedi, P.B. Littlewood, D.M. Edwards, J.Z. Sun, and J. Inoue**,** *Philos. Transact.: Math., Phys. Eng. Sci.* **365**, 1519 (1998).
2. G. Gritzner, J. Ammer, K. Kellner, V. Kavecansky, M. Mihalik, S. Matas, and M. Zentkova, *Appl. Phys. A-Mater. Science Proc.* **90**, 359 (2008).
3. Nguyen The Hiena and Nguyen Phu Thuya, *Physica B* **319,** 168 (2002).
4. Y. Kalyana Lakshmi and P. Venugopa Reddy, *J. Magn. Magn. Mater.* **321**, 1240 (2009).
5. M. Antoňák, M. Mihalik, M. Mihalik, Jr., M. Zentková, and G. Gritzner, *IEEE Trans. Magn.* **50**, 6800071 (2014).
6. Manjunath B. Bellakki, C. Shivakumara, N.Y. Vasanthacharya, and A.S. Prakash, *Mater. Res. Bull.* **45**, 1685 (2010).
7. D. Niebieskikwiat and M.B. Salamon, *Phys. Rev. B* **72**, 174422 (2005).
8. W.P. Meiklejohn and C.P. Bean, *Phys. Rev.* **102**, 1413 (1956).
9. S. Giri, M. Patra, and S Majumdar, *J. Phys.: Condens. Matter* **23**, 073201 (2011).
10. Z. Jagličić, M. Zentková, M. Mihalik, Z. Arnold, M. Drofenik, M. Kristl, B. Dojer, M. Kasunič, A. Golobič, and M. Jagodič, *J. Phys.: Condens. Matter* **24**, 056002 (2012).
11. M. Antoňák, M. Mihalik, M. Zentková, M. Mihalik, Jr., M. Vavra, J. Lazúrová, M. Fitta, and M. Balanda, *Acta Phys. Polon. A* **126**, 296 (2014).
12. D. Markovic, V. Kusigerski, M. Tadic, J. Blanusa, M.V. Antisari, and V. Spasojevic, *Scr. Mater* **59**, 35 (2008).
13. M.H. Rietveld, *J. Appl. Cryst.* **2**, 65 (1969).
14. Shilpi Karmakar, S. Taran, Esa Bose, B.K. Chaudhuri, C.P. Sun, C.L. Huang, and H.D. Yang, *Phys. Rev. B* **77,** 144409 (2008).
15. Ch. Binek, *Phys. Rev B* **70**, 014421 (2004).